Chapter 2
Direct Optical Measurement of Radial Strain in Split Hopkinson Pressure Bar Experiments

Jeremy Croom, Thomas Hannah, and Reuben Kraft

Abstract Split Hopkinson pressure bar experiments classically infer the high-strain rate mechanical properties of materials through the strain history of the incident and transmission bars. However, some materials require that the strain field history be measured directly. We present a novel method to directly measure the radial displacement of a specimen under test by reflecting monochromatic light off the specimen's surface. The radial displacement field, and thus radial strain field, can then be calculated from how the pattern of reflected light evolves during an experiment. Sources of experimental error, uncertainty, and material surface profile requirements are quantified through modeling of the specimen and viewing screen's light scattering properties. We also experimentally validate our technique using static measurements of cylindrical specimens. Lastly, feasibility for application of the technique in split Hopkinson pressure bar experiments is explored.

Keywords Strain Field Measurement · Optical Methods · Split Hopkinson Pressure Bar · Uncertainty Measurement · Reflection

Introduction

The response of materials in split Hopkinson pressure bar (SHPB) experiments is commonly inferred using one-dimensional elastic wave theory from indirect strain gauge measurements [1]. A principal assumption of these equations is stress equilibrium – a uniform stress distribution throughout the specimen. However, the behavior of some materials, like composites or soft polymers, may violate this assumption [2–4]. In turn, methods like laser occlusive radius detector (LORD) [5], photon doppler velocimetry [6], digital image correlation (DIC) [7, 8], and Moiré photography [9–11] have been developed for or extended to SHPB experiments to directly measure the specimen's strain response. The former two methods only measure local strain values, which is insufficient to resolve the material's full stress-strain response to dynamic loading. DIC and Moiré photography generate full-field strain measurements and are commonly used in experimental mechanics. Techniques that haven't been applied to SHPB experiments include coherent gradient sensing [12, 13] and fringe projection profilometry [14]. Although DIC enables direct strain measurement, the technique has some limitations and drawbacks. Chiefly, the measurement uncertainty is paced by the spatial resolution, but is also affected by speckle pattern quality, lighting, and other factors [15, 16]. Spatial resolution on the order of 10^{-2}–10^{-1} pixels [15], and therefore a minimum strain uncertainty of 10^{1}–10^{3} $\mu\varepsilon$, is commonly achieved, depending on camera resolution and specimen framing. Furthermore, single-camera DIC (e.g., 2D-DIC) methods are also susceptible to additional errors caused by out-of-plane displacement – estimated to be on the order of 10^{1}–10^{2} $\mu\varepsilon$ error for SHPB experiments, depending on specimen size, material properties, and strain [17].

Jeremy Croom
Department of Mechanical Engineering, The Pennsylvania State University, University Park, PA 1680
e-mail: jrc6940@psu.edu

Thomas Hannah
Q-DO, Los Alamos National Laboratory, SM-30 Bikini Atoll Rd, Los Alamos, NM 87545
e-mail: thannah@lanl.gov

Reuben Kraft
Department of Mechanical Engineering, The Pennsylvania State University, University Park, PA 16802
Co-Hire, Penn State Institute of Computational and Data Sciences, The Pennsylvania State University, University Park, PA 16802
e-mail: rhk12@psu.edu

© The Author(s), under exclusive license to River Publishers 2026

Motoharu Fujigaki et al. (eds.), *Advancement of Optical Methods & Digital Image Correlation in Experimental Mechanics, Volume 2, 2026*, Conference Proceedings of the Society for Experimental Mechanics Series, https://doi.org/10.13052/rp-9788743816256

Additionally, the applied speckle pattern may crack or delaminate before the completion of the SHPB experiment and terminate correlation. Moiré photography can also generate full-field strain measurements, but it requires a precise set-up and, in some cases, an application of a grating to the specimen – adding inertia and stiffness to the system [10, 18]. Furthermore, methods like the Sampling Moiré Method (SMM) can achieve displacement spatial resolution of $1/500^{th}$ the grating pitch, producing a minimum strain error of approximately $10^3 - 10^4$ $\mu\varepsilon$ [19]. In sum, these methods are not capable of capturing the full response of the material or introduce other sources of error and uncertainty that may be unacceptable.

However, the Poisson effect in materials enables an alternative method of measuring specimen strain: the radial strain is related to the axial strain by the Poisson ratio. The authors propose a method that reflects light off a nominally cylindrical specimen to create a beam pattern that can be used to measure radial displacement and thus strain. More specifically, collimated, monochromatic light will be directed at a specimen's exterior surface, which will then reflect the light as a one-dimensionally diverging beam onto a diffusively reflective viewing screen. As the divergence of the reflected beam is a function of specimen's local radius, the local intensity of the beam corresponds with the specimen's local radial strain. A camera will then capture the beam pattern off the viewing screen. The high-speed nature of SHPB experiments necessitates the use of a high-power laser illumination source and a single high-speed camera to record the data. The method can achieve similar or better accuracy as DIC methods but is not susceptible to errors associated with specimen strain.

Background

The premise of the methodology is that light directed onto the specimen will reflect off the specimen per the Law of Reflection [20]. Referring to Fig. 1, first, monochromatic light (of a single wavelength) is directed onto the specimen's exterior. Monochromatic light is preferred because reflection, scatter, and a camera's sensitivity are all wavelength dependent. The incident beam can be collimated or focused using optomechanical devices to increase the intensity of the measured beam pattern. The reflected light will diverge in accordance with the local curvature, focus or defocus due to the surface's waviness, and scatter per the surface's roughness. This reflected light is then projected onto a flat viewing screen as a wide beam pattern with a thickness of the height of the incident light beam. This pattern would be brightest where the light diverges the least, provided uniform intensity incident light and a flat viewing screen. A camera records a sequence of images of the beam reflecting off the viewing screen to capture the spatial history of the specimen's diameter. This can then be converted to radial strain.

Scattering light affects the measurements in two ways. First, the specimen's and viewing screen's surfaces will scatter the incident light, reduce the intensity of the measured reflected beam pattern, and consequently increase the measurement uncertainty. The reduction of light intensity off the specimen's surface is estimated by the total integrated scatter equation, introduced by Bennett and Porteus [21]. As shown in Equation 1, the total integrated scatter is positively correlated with rms surface roughness (σ) and negatively correlated with incident angle (θ_i) and wavelength (λ). However, given a fixed wavelength and a limited range of incident angles (a select arc of cylindrical specimen surface reflects light onto the finitely sized viewing screen), the surface roughness principally determines the quantity of specularly reflected light off the specimen. At the viewing screen, the non-Lambertian reflection reduces the intensity of light collected by the camera at higher aspecular angles (i.e., further away from the specular reflection direction). Second, the scattered light increases the signal-to-background (SB) ratio, which can degrade the accuracy of the measurement technique.

$$TIS = 1 - e^{-\left(\frac{4\pi \cos\theta_i \ \sigma}{\lambda}\right)^2} \tag{1}$$

Measurement Methodology

The sequence of captured images during an experiment contains the specimen's displacement field history. More specifically, this displacement history is extracted by recording the pixel intensity values within the beam for every image recorded and transforming the data from pixel intensity value to diameter by way of modeled relationships, as illustrated in Fig. 1(b)-(e). Examining the maximum pixel intensity value from each layer of the beam yields a one-dimensional (1D) displacement field along the axis of the specimen. Alternatively, inspecting the pixel intensity values that correspond with visible material points on the specimen's surface create a two-dimensional (2D) displacement field; however, the extent of the 2D displacement field (in the specimen's angular coordinate) is limited by the lesser of the camera's field of view and the viewing screen's size.

The relationship between intensity and specimen diameter was modeled using a simple backwards ray tracing methodology simulating specular reflection off the mirror and specimen [22]. Although the model doesn't factor it, the scattering does not significantly affect the relationship between specimen diameter and beam intensity. However, it will diminish the overall beam intensity and increase the background intensity noise. The model confirmed a monotonically increasing relationship

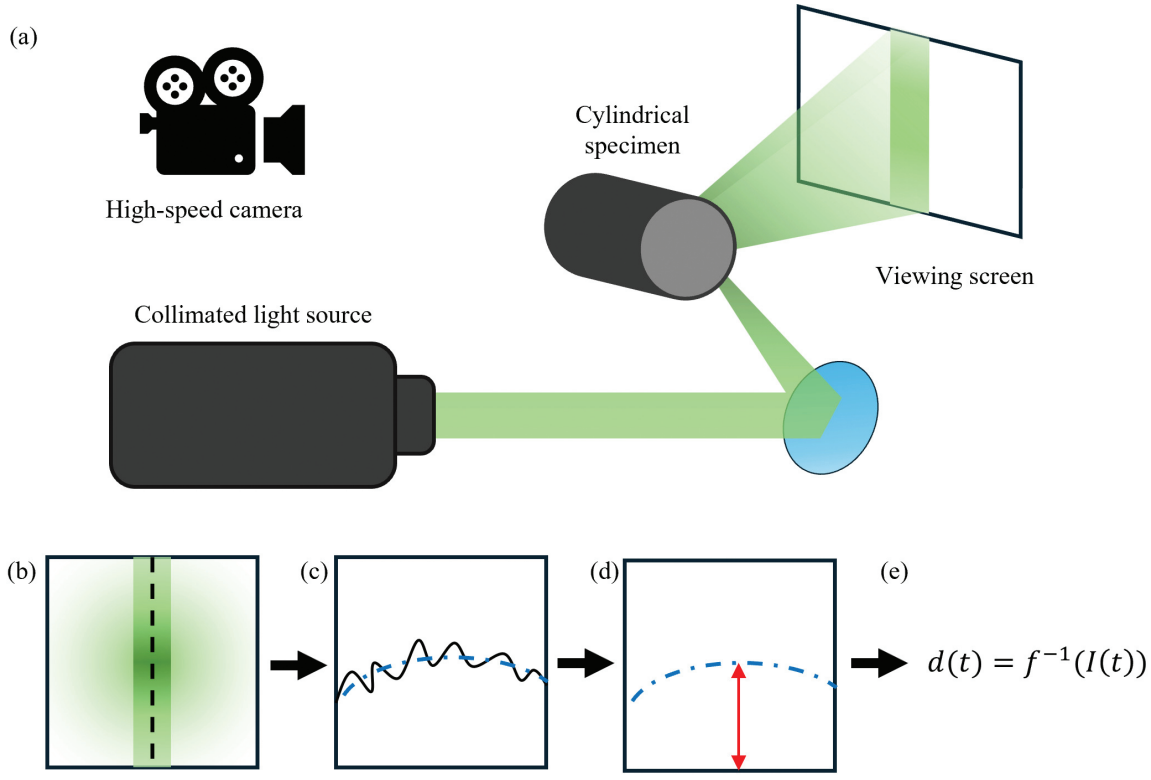

Fig. 1 (a) Illustration of reflected light pattern radial displacement optical measurement technique. The entire system is enclosed to eliminate corrupting external light sources. (b)-(e) Flowchart of process to measure specimen diameter from image. (b) Image is captured using high-speed camera. Beam intensity is measured at desired location within beam, indicated by dashed line. (c) Raw measurements are filtered to remove noise. (d) Maximum magnitude of filtered data is extracted from data. (e) Intensity is converted to diameter using a function derived from model.

between specimen diameter and intensity – linear in the case of a flat mirror. The model also identifies that the coordinate of the beam's maximum intensity on the viewing screen slightly shifts as a function of specimen diameter. Similarly, the beam coordinates of the illuminating light ray for a specific material point also changes as a function of specimen diameter and experimental geometry. A detailed discussion of the modeling findings is given in Appendix A.

Within this paper, the relationship that describes the measured pixel intensity, I, at a location on the viewing screen as a function f of the specimen diameter is generically defined as follows, with I_{rel} defined as the ratio of I to the reference (starting) pixel value, I_{ref}, and κ as a factor to scale I_{rel} to equal I:

$$I = \kappa \cdot I_{rel} = \kappa \cdot f(d) \tag{2}$$

κ is fixed for specific experimental configurations and measurement coordinates and allows the modeling to be performed independently of non-geometrical experimental parameters. Hence the inverse function to relate diameter to measured intensity is:

$$d\,(t) = f^{-1}\left(\frac{1}{\kappa} \cdot I\,(t)\right) \tag{3}$$

Static Experimental Validation

A static experiment was performed to validate the measurement concept and assess the feasibility of extending the method to SHPB tests. In this test, a CPS-532 collimated light source (Thorlabs, Newton, NJ) of wavelength 532 nm was directed with a planar mirror onto cylindrical specimens of a known diameter, which reflected a light pattern onto a viewing screen. Eight separate precision ground pin gauges (Vermont Gage, Swanton, VT) with listed diameters of 4.572 – 6.350 +0.0102/-0.0000 mm and measured rms surface roughness of 0.223 – 0.322 μm were used as specimens, representing a 32% true radial strain that may be observed in SHPB testing [23]. Surface roughness was measured in four locations on each specimen using a

VK-X3100 laser confocal optical profilometry system (KEYENCE Corporation, Osaka, Japan) with a measurement area of 286.45 x 214.76 μm (1024 x 768 pixels). Images of the reflected light pattern as reflected off the EDU-VS1 viewing screen (Thorlabs, Newton, NJ) were captured using a digital CMOS a2A4096-30umBAS camera (Basler AG, Ahrensburg, Germany) and CF8ZA-1S lens (Fujifilm, Tokyo, Japan) with a field of view of 224.4 x 164.4 mm (median 59.3 μm/pixel on viewing screen) and a sequence of exposure times (ranging from 10,000 to 900,000 microseconds). Five sets of images were collected for each specimen, totaling to 40 experiments. The experiment was configured as shown in Fig. 2(a) and Table 1. The camera is normal to the viewing screen but offset from the viewing screen's center to provide an unobscured view. For the purposes of validation, only the maximum intensity values were measured, as opposed to measuring the diameter field across the whole beam, because of hardware limitations and use of a series of specimens.

The images of every specimen were analyzed as follows to extract the maximum reflected beam pattern intensity. First, the radial and tangential distortion of the camera and lens was corrected with a distortion correction calibration procedure described by Brown and Conrady using the OpenCV library [24–27]. Experimental geometry parameters were verified and visible edges of the viewing screen were identified using a well-illuminated calibration photo. Then the pixel coordinates on the viewing screen were mapped to the physical coordinates using a pinhole camera model and the verified experimental geometry. Subsequently, all images were undistorted, scaled to a reference frame exposure time, filtered to remove saturated pixels, and averaged. Fifth, convolution, polynomial fitting, and statistical outlier detection were used to identify the location of the reflected beam pattern. The reflected beam pattern was found to be approximately 30 pixels high due to the wide camera field of view and iris diaphragm. Sixth, convolution with a uniform kernel of 1 pixel width and 15 pixels height was used in the vicinity of the detected beam to identify the brightest region of the reflected beam pattern for every column of combined image data. The maximum values were then filtered using a 3rd-order Butterworth lowpass filter with a cut-off frequency of $0.5 \cdot 10^{-2}$ 1/pixels. Seventh, the overall maximum intensity value was then extracted from the filtered data. Averaging scaled intensity values from a range of exposure times increased the effective dynamic range of the camera and minimized the effect of saturating individual pixels but would not be valid for dynamic experimentation.

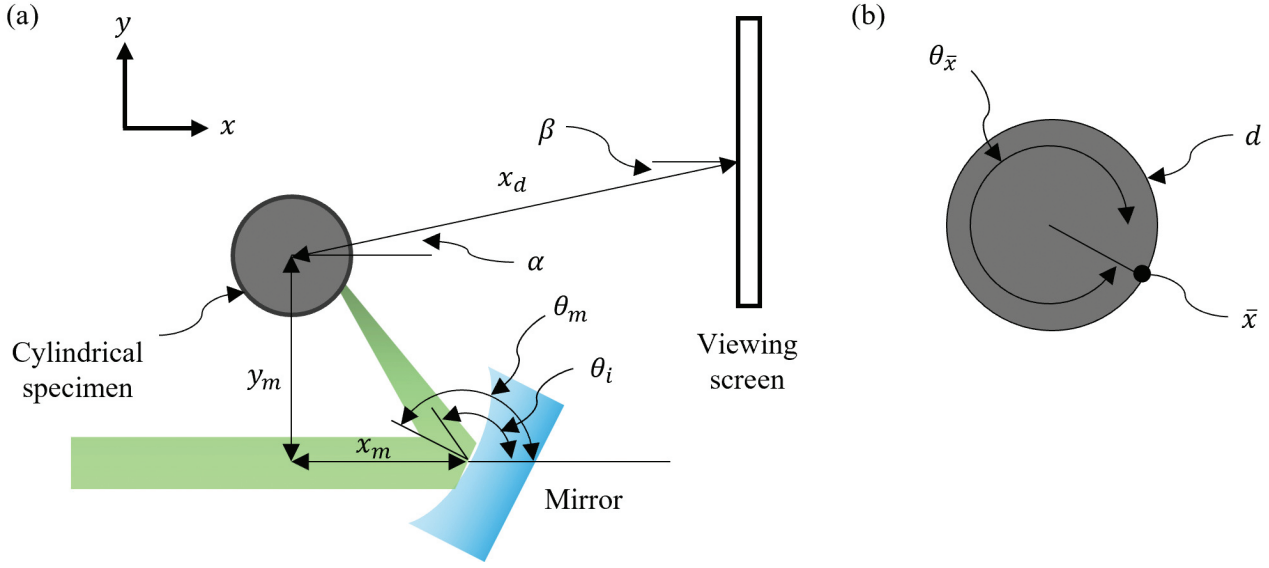

Fig. 2 Illustration of relevant 2D geometry of experiment. (a) Position and orientation of mirror and viewing screen relative to specimen. (b) Detail view of cylindrical coordinates of a material point on surface of specimen.

Results

Measurement Uncertainty

Various factors contribute to experimental uncertainty. The principal source of uncertainty is related to the camera's quantization; therefore, the bounds of radial strain uncertainty, derived from the radial true strain equation, is as shown in Equation 4. This equation could be further modified to account for uncertainty in locating the position on the viewing screen that

Table 1 Experimental Parameters

Beam Power Output	4.5 mW	Viewing Screen Dimensions	150 mm x 150 mm
Beam Diameter	3.5 mm	Viewing Screen Offset (x_d)	172.7 mm
Iris Diaphragm Diameter	1.4 mm	Viewing Screen Angle (α)	-20°
Mirror Angle (θ_m)	157.5°	Viewing Screen Orientation Angle (β)	0°
Incident Angle (θ_i)	135°	Image Size	4128 x 3008 pixels
		Image Quantization	12-bit

corresponds to the material point of interest and measuring the intensity of the illuminating light beam.

$$\epsilon(x,y,t) = \left\{ \begin{array}{l} +\left(\ln\left(\frac{f^{-1}\left(\frac{I(x,y,t)+\frac{1}{2}}{\kappa}\right)}{f^{-1}\left(\frac{I_{ref}(x,y)-\frac{1}{2}}{\kappa}\right)}\right) - \ln\left(\frac{f^{-1}\left(\frac{I(x,y,t)}{\kappa}\right)}{f^{-1}\left(\frac{I_{ref}(x,y)}{\kappa}\right)}\right)\right) \\ -\left(\ln\left(\frac{f^{-1}\left(\frac{I(x,y,t)}{\kappa}\right)}{f^{-1}\left(\frac{I_{ref}(x,y)}{\kappa}\right)}\right) - \ln\left(\frac{f^{-1}\left(\frac{I(x,y,t)-\frac{1}{2}}{\kappa}\right)}{f^{-1}\left(\frac{I_{ref}(x,y)+\frac{1}{2}}{\kappa}\right)}\right)\right) \end{array} \right\} \tag{4}$$

Given a linear relationship between radial strain, ε_{rr}, and intensity, Equation 4 can be approximated as shown in Equation 5, which reveals that the uncertainty is inversely proportional to I_{ref}: increasing the reference intensity value and/or the bit-depth will reduce the experimental uncertainty.

$$\epsilon\left(x,y,t\right) \cong \pm\frac{2-\varepsilon_{rr}(t)}{2\cdot I_{ref}(x,y)} \tag{5}$$

The uncertainty also varies spatially within the measurement field because of the following reasons. First, the reflected beam pattern will generally be a profile with a central peak and have variation due to surface waviness and scattering light. Second, the incident light beam's profile, typically Gaussian, unequally illuminates the specimen. Third, the reflected beam pattern is unequally reflected off the viewing screen into the camera – the images appear darker away from the minimum aspecular angle. Fourth, the camera lens also can affect the relative illumination of the image at the periphery. Each of these factors will reduce I_{ref} and increase the uncertainty.

Another source of uncertainty is related to the temporal variation of the light source's intensity and positional stability (inclusive of the experimental set-up's deflection), if not controlled or measured. The high-speed nature of SHPB experiments does reduce the potential temporal variation of intensity, given the small duration of experiments. Mitigations can include ensuring a constant power supply to and adequate warm-up time for the light source and simultaneously measuring the light source's intensity during the experiment.

Verification Results

A combined image from the static validation experiments is provided in Fig. 3(a) as an exemplar of typical results and to identify features within the data. The image was obtained with a specimen diameter of 4.572 mm and a reference frame exposure of 200,000 μs. The bottom-left corner of the viewing screen is approximately located at a coordinate of (460, 1,720) pixels and the bottom-right corner at (2,930, 1,730) pixels; the top of the viewing screen is outside the field of view. The reflected light pattern beam is apparent in the image, running horizontally at an approximate y-coordinate of 1,350 pixels; it is horizontal because the specimen's axis is vertical relative to the camera. Other regions of the viewing screen are illuminated because light scattering off the specimen. Additionally, a bright spot, observed at an approximate coordinate of (1,750, 1,530 pixels) corresponding to the minimum aspecular angle, dominates the image because of non-Lambertian reflection off the viewing screen. Also, a near-ellipsoidal pattern centered about the optical axis of the light source as reflected onto the viewing screen, located roughly at (1,500, 1,310 pixels) is attributed to axisymmetric intensity variation within the collimated light source (i.e., a Gaussian beam profile). Lastly, a "textural variation" in the apparent intensity is attributed to the waviness of the specimen and constructive and destructive interference caused by its surface profile.

The reflected light pattern beam was processed to extract the maximum intensity from the beam using the described procedure. The corresponding extracted beam intensity plot for Fig. 3(a) is shown in Fig 3(b). Significant noise is observed within the measurements; however, the filtered data removes most of the noise and reveals a more useable measurement. Nevertheless, in comparison to the modeled intensity, there is a minor discrepancy between the two intensity profile shapes. More specifically, the magnitude of the measured intensity is at its maximum at the minimum aspecular angle and declines away. The modeled intensity only gradually declines away from its maximum, which is located at an x-coordinate of approximately 1,400 pixels. This difference is because the model measures the relative intensity of the light incident on the viewing screen. Regardless, as the location of the incident maximum intensity shifts negligibly over the course of the experiment (approximately 5 pixels), this discrepancy will have a negligible effect on the overall maximum intensity value of the reflected beam pattern.

The results from each of the 40 experiments are summarized in Fig 4(a). The maximum filtered beam intensity values are shown in blue, and the mean intensity measured on the screen is shown in red. The mean screen intensity is used as a proxy measure for the total quantity of light reflected off the finitely sized viewing screen. Both sets of data are fitted with a linear regression, in accordance with theory and the diameter-intensity model. Pearson correlation coefficients for the beam maxima and mean screen intensity are 0.62 and 0.64. The 5.334 mm diameter specimen, the smoothest of all specimens, consistently exhibited nearly double the predicted reflected secular intensity over all experimental set-ups. It had a mean sq value of 0.225 μm, compared to a mean sq of 0.268 μm for the entire set of specimens. Correspondingly, per TIS theory, this specimen would be expected to have a higher specular reflectance than the other specimens, affecting the apparent correlation. However, when omitting this specimen, the beam maxima and mean screen intensity have Pearson correlation coefficients of 0.89 and 0.77. The high correlation supports the theory that beam intensity is proportional to specimen diameter.

Additionally, the mean maximum SB ratio of the reflected pattern beam was 2.94 with a standard deviation of 0.55. The 5.334 mm diameter specimen, with its smoother surface, also had the largest maximum SB ratio of 3.61. At the edges of the viewing screen, with the dimmest beam intensity, a mean SB ratio of the reflected pattern beam was 1.05 with a standard deviation of 0.38. Per Equation 1, the specimens would be expected to scatter over 99.99% of their light, which strongly contributes to the low SB ratio. However, as noted by Harvey, the intensity of the specular reflected beam pattern will increase significantly for specimens with a relevant roughness satisfying the criteria $\frac{\sigma_{rel}}{\lambda} < 0.16$ [28]. For this experiment, the limit for surface finish would be $\sigma_{rel} = 0.086$ μm. Furthermore, the exponential nature of Equation 1 suggests that small improvements to the surface roughness would yield a specular reflected beam pattern orders of magnitude more intense than found in this experiment. In comparison to the specimens utilized, smoother surfaces will be required to enable the measurement of a 2D displacement field.

The fitted intensity model $\hat{I}(\hat{d})$ can then be used to calculate the error of the experiment. The predicted diameter can be found using Equation 6 to solve for the valid root $\hat{d}$ (i.e., the predicted diameter), where $I\,(d_0)$ is the measured intensity of the specimen diameter of interest.

$$I\,(d_0) = \hat{I}(\hat{d}) \tag{6}$$

Then, the percentage error can be found using Equation 7.

$$\epsilon\,(d_0) = \frac{\hat{d} - d_0}{d_0} \cdot 100\% \tag{7}$$

The average error of the predicted diameter using maximum filtered intensity values was found to be 9.4%, with a maximum error of 34.9% associated with a diameter of 5.334 mm. The average error of the predicted diameter using mean screen intensity values was found to be 10.1%, with a maximum error of 23.4% associated with a diameter of 5.334 mm. The main source of error is surmised to be the varying surface roughness of the specimens because the smoother specimens consistently generated higher measured intensities than predicted by the model, as shown in Fig 4(b), even over multiple experiments. In addition to the varying surface roughness values, variation in the experimental results is also affected by the geometrical alignment of the specimens relative to the light source. Observation of the raw images indicates that the placement of the specimens varied by up to 1 mm in the horizontal plane. The observed range of specimen placement, coupled with the Gaussian intensity profile of the collimated light source (beam diameter of 3.5 mm), predicts a 20% variation of in measured maximum intensity and a predicted diameter error of up to 10%. Therefore, the experimental error, after discounting the 5.334 mm diameter specimen, can be explained by the varying surface roughness and placement of the specimens.

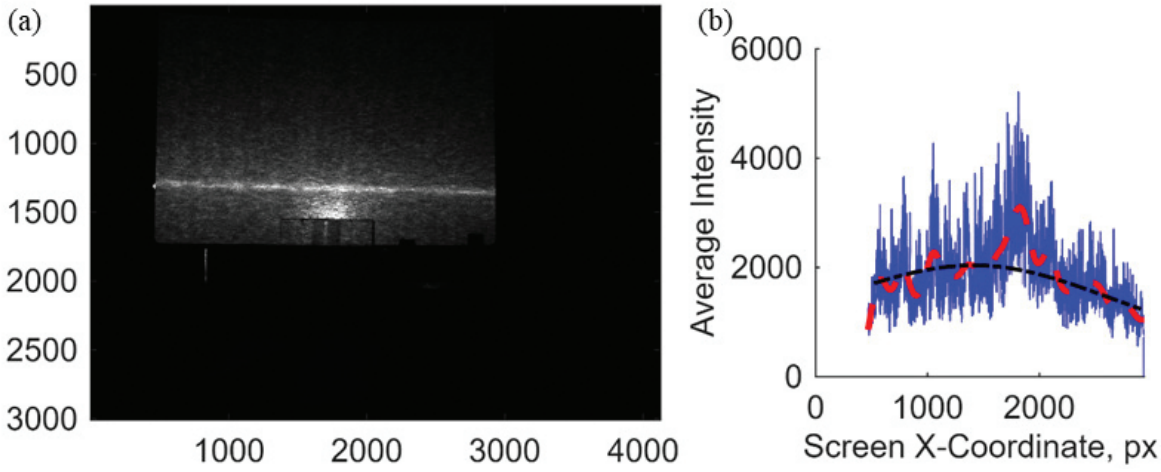

Fig. 3 (a) Combined image from static validation experiment with specimen diameter of 4.572 mm and frame exposure of 200,000 µs. The x and y axes of the image are identified. (b) Measured intensity of beam from static validation experiment with specimen diameter of 4.572 mm and frame exposure of 200,000 µs. Raw intensities (blue) for every image column were averaged over a height of 15 pixels and filtered (red dashes) using a 3rd-order Butterworth filter. Modeled intensities, scaled to match the measured data, are shown for comparison (black dash dots).

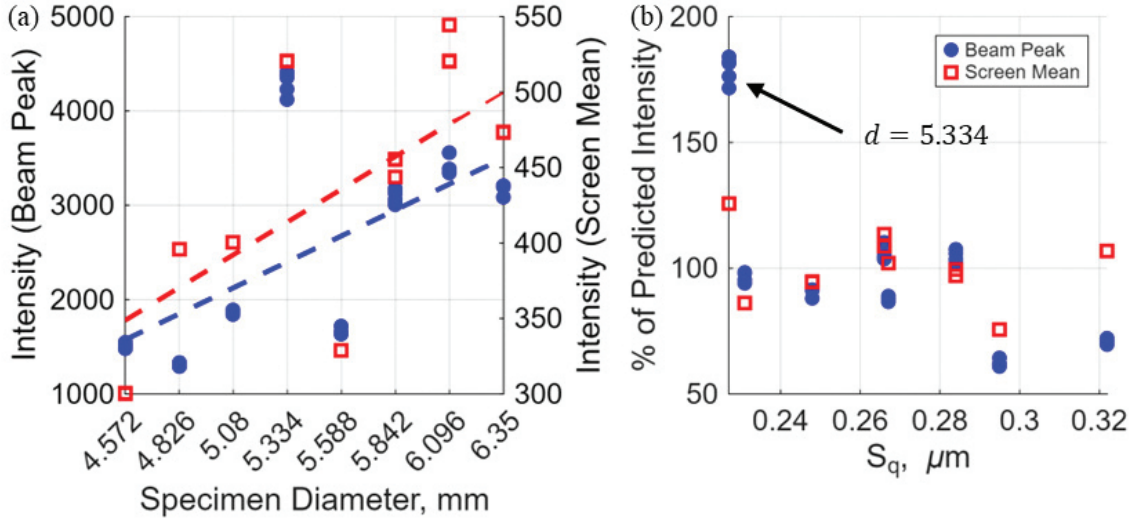

Fig. 4 (a) Measured pixel intensity values of reflected light pattern beam for 40 static validation experiments. Beam Peak (blue) is the maximum filtered intensity value and Screen Mean (red) is the mean intensity value on the entirety of the viewing screen. (b) Measured intensity values as percentage of predicted intensity values.

Discussion

The reflected light pattern measurement technique compares favorably to other measurement methods. First the method achieves accuracy similar to or better than DIC and SMM. Equation 5 demonstrates that the reflected light pattern measurement technique can achieve a measurement uncertainty no better than 978 radial $\mu\varepsilon$ with 10 bit-depth high-speed cameras used in SHPB experiments, in line with the upper bounds of DIC and SMM strain uncertainty of 10^3 $\mu\varepsilon$ and 10^4 $\mu\varepsilon$ respectively [7, 8]. Higher bit-depth cameras can also improve the uncertainty of the measurement. Additionally, the method is minimally sensitive to out-of-plane displacement. Second, the method is suitable for high-throughput testing, as specimens can be prepared in bulk, albeit made with more stringent surface roughness tolerances, and then used immediately thereafter. DIC, however, requires a speckle pattern and Moiré methods, a delicate grating, to be first applied. The manufacture and application of grating systems can become difficult for small bar diameter SHPB systems.

The method does have some drawbacks as well. First, the method requires surface roughness tolerances that are more stringent than typically used in SHPB experiments, as the surface roughness affects both the selection of a light source and the SB ratio. Although there are methods that can achieve these tolerances, this requirement does affect the economic viability of the method. Second, the 1D spread of the reflected pattern beam necessitates a trade-off of spatial resolution in the axial or circumferential directions. For instance, focusing a camera in on a central portion of the reflected beam pattern limits the measurement to a narrow surface arc of the specimen. Contrarily, DIC and Moiré methods can capture information across an entire face of a specimen. Third, the light source's power variation needs to be controlled or measured to minimize measurement uncertainty.

The results from the static validation experiments confirm the viability of the experimental method in SHPB experiments. As the surface roughness would be held nearly constant for an intact specimen and the alignment of the light source, specimen, viewing screen, and camera would be virtually constant throughout an experiment, the observed errors from the static experiment are not expected. Specimens will require similar, if not better surface roughness (i.e., $\frac{\sigma_{rel}}{\lambda} \leq 0.375$) than what was used during the static experiment, as well, and approaching 0.16 to enable 2D displacement field measurements. Drawing upon the Generalized Harvey-Shack scattering theory, factors such as surface roughness, correlation width, and reflectivity affect the intensity of the reflected beam and the bidirectional reflectance distribution function – and thus the SB ratio [29–31]. The significantly faster frame rates to capture SHPB experiments (e.g., $10^5 - 10^6$ FPS) encourages the use of, but does not necessitate, better surface roughness values, as image brightness can also be increased through experimental set-up (such as using cylindrically concave mirrors to focus light onto the specimens or using a more powerful light source). For metallic specimens, finishing methods such as polishing, surface grinding or electropolishing can decrease the scatter. For polymeric specimens, polishing or surface grinding can also decrease the scatter. However, many polymeric materials have low reflectance, so an application of a high reflectance coating may be necessary.

Conclusion and Future Work

The authors introduced a novel methodology to measure specimen diameter and radial strain fields during dynamic experiments, such as SHPB tests, using the light pattern reflected off the specimen's surface. Additionally, modeling confirmed the relationship between specimen diameter and measured intensity and revealed insights into the influence of experimental parameters. The uncertainty in measuring strain was characterized using the modeled relationships and was found to be fundamentally related to image quantization. Then, using procedures outlined above, the model and experimental method were validated using a static experiment and ground steel cylinders. Lastly, the experimental results identify a recommended maximum surface roughness value to obtain satisfactory image brightness and SB ratios.

Two limitations of the experimental method are that the specimens need to be sufficiently reflective and smooth to obtain usable reflected patterns. As such, future work will explore surface treatments and coatings to expand the technique to other materials (e.g., polymers or fiber-reinforced composites) and to lessen machining requirements. Additionally, the authors would like to scale up this measurement method to a SHPB experiment to fully demonstrate its potential.

Appendix A

Modeling the experiment using the reverse ray tracing methodology revealed insights into experimental parameters such as light source intensity distribution, mirror curvature and placement, and viewing screen placement. Sample results from the modeling are included below. Fig A1(a) confirms a linear relationship between specimen diameter and the maximum measured relative intensity; however, this relationship is not necessarily linear when using a cylindrically concave mirror to focus incident light onto the specimen. This plot also highlights that the reflected beam pattern is more intense as the light incident angle approaches the viewing screen angle (in this case $\theta_i = 160^\circ$), although this is limited by the apparent width of the viewing screen and the physical size of components, as to not obscure the incident light. In contrast Fig A1(e) demonstrates that the intensity pattern shifts dramatically, emphasizing that relative intensity is also a function of the incident light intensity profile. Fig A1(b) establishes that the coordinates on the viewing screen of the beam's maximum intensity also slightly changes with the specimen's diameter and more significantly based on the incident angle. Comparatively, Fig A1(f) highlights that these coordinates can shift more significantly for non-uniform illumination. These four figures show that there is some sensitivity to the alignment of the experiment, although the variation in light source alignment is expected to be minimal during an experiment. As expected for a uniformly intense illumination Fig A1(c) and (d) illustrate how the intensity and coordinates of the maximum brightness are insensitive to specimen misalignment. However, Fig A1(g) and (h)

show how specimen misalignment can affect the intensity and coordinates of the maximum intensity when nonuniformly illuminated. Collectively, the modeling underlines the importance of careful selection and control of experimental parameters to maximize the accuracy of the experiment.

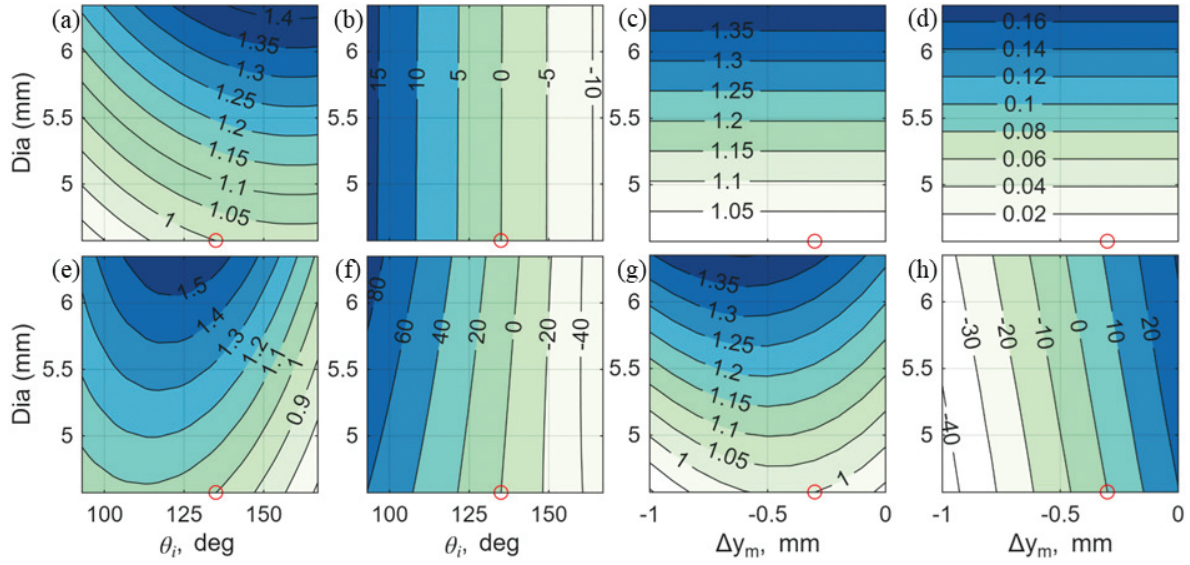

Fig. A1 Predicted intensity and coordinates of reflected beam pattern modeling using collimated light of uniform intensity. (a) Contour plot of the normalized intensity values for uniform illumination as a function of incident angle and specimen diameter. (b) Contour plot of the relative coordinate of the maximum brightness for uniform illumination as a function of incident angle and specimen diameter. (c) Contour plot of the normalized intensity values for uniform illumination as a function of specimen position and specimen diameter. (d) Contour plot of the relative coordinate of the maximum brightness for uniform illumination as a function of specimen position and specimen diameter. (e)-(h) Contour plots of above, but with Gaussian illumination.

Acknowledgments The research reported here was funded by Los Alamos National Laboratory (Subcontract No. 587178; Funder ID: 10.13039/100008902). The authors would like to thank Dr. Thomas Hannah of Los Alamos National Laboratory for assistance with the modeling process and providing administrative support during the contracting process. The authors would also like to thank Dr. Akhlesh Lakhtakia for providing experimental facilities and Dr. Tim Tighe for instruction on the operation of optical profilometry systems, both of Pennsylvania State University.

References

1. Kolsky, H., "An investigation of the mechanical properties of materials at very high rates of loading," P. Phys. Soc. Lond. B, 62, pp. 676–700, 1949. doi:10.1088/0370-1301/62/11/302.
2. Hannah, T., "Development of kolsky bar techniques and the experimental characterization of ultra high molecular weight polyethylene composites," The Pennsylvania State University, 2023.
3. Chen, W., Zhang, B., Forrestal, M. J., "A split hopkinson bar technique for low-impedance materials," Exp. Mech., 39, pp. 81-85, 1999. doi:10.1007/BF02331109.
4. Johnson, T. P. M., Sarva, S. S., Socrate, S., "Comparison of low impedance split-hopkinson pressure bar techniques in the characterization of polyurea," Exp. Mech., 50, pp. 931–940, 2010. doi:10.1007/S11340-009-9305-Y.
5. Li, Y., Ramesh. K. T., "An optical technique for measurement of material properties in the tension kolsky bar," Int. J of Impact Eng., 34, pp. 784-798, 2007. doi:10.1016/j.ijimpeng.2005.12.002.
6. Casem, D. T., Zellner, M. B., "Measurements of particle velocity within a kolsky bar with applications to wave separation," in C. Proc. Soc. Exp. Mech., V. Chalivendra, B. Song, D. Casem, eds., Springer New York, New York, NY, pp. 57–65, 2013. doi:10.1007/978-1-4614-4238-7_8.
7. Lawlor, B. P., Gandhi, V., Ravichandran, G., "An internal digital image correlation technique for high-strain rate dynamic experiments," Exp. Mech., 65, pp. 407–419, 2025. doi:10.1007/s11340-025-01149-2.
8. Sutton, M. A., Gilat, A., Seidt, J., et al., "Full field deformation measurements in tensile kolsky bar experiments: studies and detailed analysis of the early time history," J of Dyn. Beh. of Mats., 4, pp. 95–113, 2018. doi:10.1007/s40870-017-0140-4.
9. Melin, L. G., Thesken, J. C., Nilson, S., Benckert, L. R., "Tensile impact delamination of a cross-ply interface studied by moiré photography," Fatigue Fract. Eng. M., 18, pp. 1101–1114, 1995. doi:10.1111/j.1460-2695.1995.tb00842.x.

10. Melin, L. G., Asp, L. E., “Effects of strain rate on transverse tension properties of a carbon/epoxy composite: studied by moiré photography,” Compos. Part A - Appl. S., 30, pp. 305–316, 1999. doi:10.1016/S1359-835X(**??**)00123-7.
11. Xia, K., Yao, W., “Dynamic rock tests using split hopkinson (kolsky) bar system - a review,” J Rock Mech. and Geo. Eng., 7, pp. 27–59, 2015. doi:10.1016/j.jrmge.2014.07.008.
12. Tippur, H. V., Krishnaswamy, S., Rosakis, A. J., “A coherent gradient sensor for crack tip deformation measurements: analysis and experimental results,” Int J Fract, 48, pp. 193–204, 1991. doi:0.1007/BF00036631.
13. Tippur, H. V., “Coherent gradient sensing (CGS) method for fracture mechanics: A review,” Fatigue Fract. Eng. M., 33, pp. 832–858, 2010. doi:10.1111/j.1460-2695.2010.01492.x.
14. Xu, J., Zhang, S., “Status, challenges, and future perspectives of fringe projection profilometry,” Opt. Lasers Eng., 135, p. 106193, 2020. doi:10.1016/j.optlaseng.2020.106193.
15. Bomarito, G. F., Hochhalter, J. D., Ruggles, T. J., Cannon, A. H., “Increasing accuracy and precision of digital image correlation through pattern optimization,” Opt. Lasers Eng., 91, pp. 73–85, 2017. doi:10.1016/j.optlaseng.2016.11.005.
16. Schreier, H., Orteu, J. J., Sutton, M. A., “Practical considerations for accurate measurements with DIC,” in Image Correlation for Shape, Motion and Deformation Measurements: Basic Concepts, Theory and Applications,” Springer US, New York, NY, pp. 229-252, 2009. doi:10.1007/978-0-387-78747-3.
17. Sutton, M. A., Yan, J. H., Tiwari, V., et al., “The effect of out-of-plane motion on 2D and 3D digital image correlation measurements,” Opt Lasers Eng, 46, pp. 746–757, 2008. doi:10.1016/j.optlaseng.2008.05.005.
18. Ritter, R., “A dynamic moiré method for deformation measurement of curved surfaces,” Exp. Mech., 19, pp. 145–146, 1979. doi:10.1007/BF02324227.
19. Ri, S., Fujigaki. M., Morimoto, Y., “Sampling moiré method for accurate small deformation distribution measurement,” Exp. Mech., 50, pp. 501–508, 2010. doi:10.1007/s11340-009-9239-4.
20. Yu, N., Genevet, P., Kats, M. A., et al., “Light propagation with phase discontinuities: generalized laws of reflection and refraction,” Science, 334, pp. 333–337, 2011. doi:10.1126/science.1210713.
21. Bennett, H. E., Porteus J. O., “Relation between surface roughness and specular reflectance at normal incidence,” J. Opt. Soc. Am., 51, 123–129, 1961. doi:10.1364/JOSA.51.000123.
22. Arvo, J., “Backward ray tracing,” in Comp. Graph, A. Barr, ed., pp 259–263, 1986.
23. Holmquist, T. J., Bradley, J., Dwivedi. A., Casem, D., “The response of polymethyl methacrylate (PMMA) subjected to large strains, high strain rates, high pressures, a range in temperatures, and variations in the intermediate principal stress,” Eur. Phys J-Spec. Top., 225, pp. 343–354, 2016. doi:10.1140/epjst/e2016-02636-5.
24. Brown, D. C., “Close-range camera calibration,” Photogramm. Eng., 37, pp. 855–866, 1971.
25. Brown, D. C., “Decentering distortion of lenses,” Photogramm. Eng., 32, pp. 444–462, 1966.
26. Conrady, A. E., “Decentered lens-systems,” Mon. Not. R. Astron. Soc., 79, pp. 384–390, 1919. doi:10.1093/mnras/79.5.384.
27. Open Source Vision Foundation, “The opencv library (Version 4.12.0)”, Open Source Vision Foundation, Palo Alto, CA, 2025.
28. Harvey, J. E., Choi, N., Krywonos, A., et al., “Calculating BRDFs from surface PSDs for moderately rough optical surfaces,” in P. Soc, Photo.-Opt. Ins., J. Burge, O. Fähnle, R. Williamson, eds., SPIE, Bellingham, WA, pp. 141–149, 2009. doi:10.1117/12.831302.
29. Krywonos, A., “Predicting surface scatter using a linear systems formulation of non-paraxial scalar diffraction,” The University of Central Florida, 2006.
30. Harvey, J. E., Krywonos, A., Stover, J. C., (2007) “Unified scatter model for rough surfaces at large incident and scatter angles,” in P. Soc, Photo.-Opt. Ins., A. Duparré, B. Singh, Z. Gu, eds., SPIE, Bellingham, WA, pp. 103–110, 2007. doi:10.1117/12.739139.
31. Krywonos, A., Harvey, J. E., Choi, N., “Linear systems formulation of scattering theory for rough surfaces with arbitrary incident and scattering angles,” J. Opt. Soc. Am. A, 28, pp. 1121–1138, 2011. doi:10.1364/JOSAA.28.00112.